Strategies for Doped Nanocrystalline Silicon Integration in Silicon Heterojunction Solar Cells

Johannes P. Seif, Antoine Descoeudres, Gizem Nogay, Simon Hänni, Silvia Martin de Nicolas, Niels Holm, Jonas Geissbühler, Aïcha Hessler-Wyser, Martial Duchamp, Rafal E. Dunin-Borkowski, Martin Ledinsky, Stefaan De Wolf, and Christophe Ballif

***Abstract*—Carrier collection in silicon heterojunction (SHJ) solar cells is usually achieved by doped amorphous silicon layers of a few nanometers, deposited at opposite sides of the crystalline silicon wafer. These layers are often defect-rich, resulting in modest doping efficiencies, parasitic optical absorption when applied at the front of solar cells, and high contact resistivities with the adjacent transparent electrodes. Their substitution by equally thin doped nanocrystalline silicon layers has often been argued to resolve these drawbacks. However, low-temperature deposition of highly crystalline doped layers of such thickness on amorphous surfaces demands sophisticated deposition engineering. In this paper, we review and discuss different strategies to facilitate the nucleation of nanocrystalline silicon layers and assess their compatibility with SHJ solar cell fabrication. We also implement the obtained layers into devices, yielding solar cells with fill factor values of over 79% and efficiencies of over 21.1%, clearly underlining the promise this material holds for SHJ solar cell applications.**

***Index Terms*—Microcrystalline silicon, nanocrystalline silicon, silicon heterojunctions (SHJs), solar cells.**

I. Introduction

HYDROGENATED nanocrystalline silicon (μc-Si:H) deposited by plasma-enhanced chemical vapor deposition (PECVD) features nanometer-sized silicon crystals embedded in an amorphous silicon (a-Si:H) matrix. This material has already been studied for several decades and found its way into several important applications including photovoltaic devices [1]–[8], thin-film transistors [9], and microelectromechanical systems [10]. Significant effort was put on the experimental [11]–[16] and theoretical [17] investigation of its growth process [4], [18], as well as its electrical [19]–[21] and optical properties [2], [15].

In the case of solar cells, μc-Si:H was for a long time mainly used as absorbing material of the bottom cell in so-called micromorph silicon thin-film tandem devices [2], [22], motivated by its favorable absorption coefficient in the red part of the solar spectrum as compared with a-Si:H [2], [7], [15]. More recently, μc-Si:H and nanocrystalline silicon oxide (μc-SiO_x:H) have also been investigated for application in amorphous/crystalline silicon heterojunction (SHJ) solar cells [3], [5], [7], [8], [23], [24]. Device integration of these layers has the potential to improve further the already very high conversion efficiencies achieved to date of up to 25.1% for two-side-contacted and 25.6% for interdigitated back-contacted SHJ cells, obtained with presumably all-amorphous layers [25], [26]. Indeed, its reduced absorption at shorter wavelengths, linked to its indirect bandgap, makes μc-Si:H an ideal candidate for window layers that could enable an increase of the short-circuit current density (J_{sc}) [15]. Furthermore, its higher doping efficiency and its improved transport properties [20], [27], [28] compared with a-Si:H [19], [20], [29]—its potentially lower contact resistivity in particular—could help to increase the fill factor (*FF*). In fact, μc-Si:H has been reported to suppress Schottky barriers that are prone to form at the interface with the adjacent transparent conductive oxides (TCO) [7], [8], [29], [30].

For silicon thin-film tandem devices, where the thickness of the μc-Si:H bottom cell is in the order of micrometers, the deposition conditions are usually optimized towards high bulk material quality and high deposition rates [31], [32]. For SHJ devices—featuring layers in the order of ten nanometer or less—[33] additional requirements apply. These are: 1) fast nucleation and suppression of an a-Si:H incubation layer [15] irrespective of the substrate morphology and chemistry [34], [35], as such incubation layers diminish the expected gains in J_{sc} and *FF*; 2) sufficiently high Raman crystallinity (χ_c) to benefit from improved optical and transport properties; and 3) "soft" deposition, without degrading the underlying intrinsic a-Si:H passivation layer or damaging the wafer interface. This intrinsic buffer layer, including its interface with the crystalline silicon

Manuscript received December 10, 2015; revised March 17, 2016 and May 5, 2016; accepted May 13, 2016. Date of publication June 20, 2016; date of current version August 18, 2016. This work was supported by the EuroTech University Alliance in the framework of the Interface Science for Photovoltaics initiative, by the Swiss Commission for Technology and Innovation under Grant 13348.1, by Axpo Naturstrom Fonds, by the European Commission (FP7 project HERCULES, Grant 608498; FP7 project CHEETAH, Contract 609788; FP7 contract for an Integrated Infrastructure Initiative, 312483-ESTEEM2), by the Office fédéral de l'énergie, by the Fonds National Suisse Reequip program under Grant 206021_139135 and Grant 206021_133832, by the DOE project FPaceII, and by the Czech Ministry of Education, Youth and Sports Project LM2011026.

J. P. Seif, G. Nogay, S. Hänni, S. M. de Nicolas, N. Holm, J. Geissbühler, A. Hessler-Wyser, S. De Wolf, and C. Ballif are with the Photovoltaics and Thin-Film Electronics Laboratory, Institute of Microengineering, Ecole Polytechnique Fédérale de Lausanne, Neuchâtel 2000, Switzerland (e-mail: johannes.seif@alumni.epfl.ch; gizem.nogay@epfl.ch; sh.pvlab@gmail.com; silvia.martin-de-nicolas@epfl.ch; niels.holm@epfl.ch; jonas.geissbuehler@epfl.ch; aicha.hessler@epfl.ch; stefaan.dewolf@epfl.ch; christophe.ballif@epfl.ch).

A. Descoeudres is with the Centre Suisse d'Electronique et de Microtechnique, Neuchâtel 2000, Switzerland (e-mail: antoine.descoeudres@csem.ch).

M. Duchamp and R. E. Dunin-Borkowski are with the Ernst Ruska-Centre for Microscopy and Spectroscopy with Electrons and Peter Grünberg Institute, Forschungszentrum Jülich, Jülich 52425, Germany (e-mail: m.duchamp@fz-juelich.de; r.dunin-borkowski@fz-juelich.de).

M. Ledinsky is with the Laboratory of Nanostructures and Nanomaterials, Institute of Physics, Academy of Sciences of the Czech Republic, Prague 162 00, Czech Republic (e-mail: ledinsky@fzu.cz).

Color versions of one or more of the figures in this paper are available online at http://ieeexplore.ieee.org.

Digital Object Identifier 10.1109/JPHOTOV.2016.2571619

substrate, is one of the most sensible and crucial parts of the device. Its passivation properties enable very high operating voltages and, hence, the high efficiencies previously mentioned [36]. Therefore, considering the requirements listed here, the implementation of μc-Si:H layers is generally considered to be challenging as their deposition conditions can degrade the passivation and as it is difficult to ensure high χ_c values for layers in the range of 10 nm. This thickness requirement applies mainly to layers integrated at the front of the device. However, it is less stringent for application of μc-Si:H layers at the rear, at least for monofacial devices. Indeed, both the deposition-associated high hydrogen dilution and plasma power can potentially lead to layer modification or etching [37]. Furthermore, boron addition to the process gases inhibits nanocrystalline growth [38], [39], hence hindering fast nucleation for *p*-doped layers.

Various groups have reported approaches to minimize incubation layers, and excellent results have been obtained by optimizing the deposition parameters (temperature, pressure, power, silane dilution, frequency) [11], [18], [32], [40]. Pretreatments of the surface or deposition of buffer layers have also been explored, to induce fast nucleation [8], [41], [42]. Furthermore, specific deposition procedures, like the sequential deposition/etching (layer-by-layer) method, have been applied successfully [43], [44].

In this paper, we focus specifically on the integration of boron-doped [μc-Si:H(*p*)] and phosphorous-doped [μc-Si:H(*n*)] layers into SHJ solar cells, while satisfying the requirements mentioned above. This paper outlines strategies to obtain ultrathin nanocrystalline silicon films applicable for SHJ solar cell fabrication but mentions also the unsuccessful approaches that result in poor device performance. Due to the amorphizing impact of boron on layer growth [39], we specifically focus on *p*-type μc-Si:H layers. We also report cell results obtained with both *p*- and *n*-doped μc-Si:H layers deposited using different plasma regimes and with different device architectures.

II. Experiments

All the experimental results shown here were obtained with either a medium-area research PECVD tool (KAI-M, developed at TEL Solar) powered at a frequency of 40.68 or 13.56 MHz, or a small-area PECVD cluster tool (INDEOtec Octopus I) with chambers powered at frequencies between 13.56 and 81.36 MHz, or combining both systems sequentially (*e.g.,* a-Si:H layers in KAI-M and μc-Si:H layers in Octopus I). The gases used for the depositions were silane (SiH_4), disilane (Si_2H_6), silicon tetrafluoride (SiF_4), hydrogen (H_2), deuterium (D_2), carbon dioxide (CO_2), trimethylborane [$B(CH_3)_3$, TMB, diluted in H_2 at 0.05%], phosphine (PH_3, diluted in H_2 at 2%), and, in some cases, argon (Ar). For material development purposes, the μc-Si:H layers were either deposited directly on glass or on a-Si:H-coated glass. Further details on the deposition equipment and the processes used for fabrication of cells can be found elsewhere [45]–[47].

The layers were characterized by spectroscopic ellipsometry (SE, HORIBA Jobin Yvon, UVISEL) fitting the data using a model similar to the one described in [48]. Furthermore, Raman spectroscopy [1) Renishaw RAMASCOPE, green laser at 514 nm, and 2) Renishaw InVia REXLEX, UV laser at 325 nm] was used for layer characterization. With a penetration depth in the range of 10 nm, the UV laser allowed for direct measurements of the layers on textured wafers, while the green laser (penetration depth in the range of 150 nm) was used for layer characterization on glass substrates. The Raman spectra were deconvoluted using three Gaussian peaks centered at 480, 510, and 520 1/cm, which are often attributed to the amorphous phase, small-sized grains, or grain boundaries and the bulk crystalline phase, respectively [49]. The χ_c values were determined from the ratio of the areas A_i below the Gaussian peaks:

$$\chi_c = \frac{(A_{510} + A_{520})}{(A_{480} + A_{510} + A_{520})}. \quad (1)$$

For layers thicker than 20 nm, the thickness was also measured by profilometry (Ambios XP-2). Note that the thickness values given here correspond to the thickness determined on flat substrates.

Selected layers were deposited on a-Si:H-coated, double-side polished wafers with (1 1 1) crystallographic orientation. Polished wafers were used to facilitate the subsequent analysis of the transmission electron microscopy (TEM) micrographs. These samples were processed into cross-sectional specimen by focused ion beam milling for high-resolution TEM investigations. A final thinning step was performed with low energy Ar ions (0.5 eV) using a Fischione NanoMill system. Structural investigations were performed using an FEI Titan microscope equipped with a spherical aberration corrector at the image plane with a beam energy of 300 kV.

In a later step, selected layers were implemented into SHJ devices. Sputtered indium tin oxide electrodes were used at both the front and rear of the solar cells with carrier densities in the range of 10^{19}–10^{20} $1/\mathrm{cm}^3$ and carrier mobilities of 20–30 $\mathrm{cm}^2/\mathrm{Vs}$. Blanket silver was deposited as metallization at the rear by sputtering, whereas a screen-printed grid was used at the front applying a low-temperature silver paste cured at around 200 °C. The finished cells were characterized in-house, with a four-probe current-voltage (*J*-*V*) setup placed under an AAA solar simulator operated at standard conditions (25 °C, AM1.5g spectrum, 1000 W/m^2) and suns-V_{oc} (Sinton Instruments, [50]). All wafer-based samples were monitored in terms of effective minority-carrier lifetime (τ_{eff}, WCT-100, Sinton Instruments)—giving access to the implied operating voltages in open-circuit conditions (iV_{oc}) and at the implied maximum-power point (iV_{mpp})—and by PL imaging for qualitative lifetime mapping. The EQE and reflectance (*R*) were measured and the IQE calculated accordingly using an IQE-SCAN setup (pv-tools).

III. Results and Discussion

A. Surface Treatments and Nucleation Layers

1) Intrinsic Amorphous Silicon Oxide Buffer Layers: An approach to modify the surface of the a-Si:H layer prior to μc-Si:H(*p*) layer deposition, with as aim to facilitate nucleation—similarly to CO_2 treatments proposed and used by other authors [41], [51]–[53]—is the deposition of a

hydrogenated amorphous silicon oxide (a-SiO_x:H) buffer layer. Here we used SiH_4 and CO_2, highly diluted in H_2 ($[SiH_4/H_2] = 0.003$) [42]. We tested this for a μc-Si:H(p) process at 40.68 MHz yielding a layer with a χ_c of approximately 50% for a thickness of 60 nm, when deposited directly on glass (reference sample). Nevertheless, the deposition of this material on a-Si:H(i)-coated glass, using the same plasma parameters, did not yield nanocrystalline material. The insertion of a thin (<1 nm thick) a-SiO_x:H buffer layer, however, led to comparable χ_c values as obtained for the reference sample. Interestingly, this thin layer of a-SiO_x:H is sufficient to drastically improve the nucleation [35]. Despite this promising result, implementation into devices yielded strongly s-shaped *J-V* curves (data not shown here). Even though insufficient layer thickness, crystallinity, or doping have to be considered as potential cause, we suspect the presence of a barrier for the holes introduced by the a-SiO_x:H layer as the culprit. Similar oxide-related barriers were found to impede hole transport in the past [46], [54], [55].

2) Nanocrystalline Nucleation Layers Deposited by Silicon Tetrafluoride Plasma Chemistry: Nanocrystalline silicon deposited by SiF_4 and H_2 highly diluted in Ar has been found to exhibit very high χ_c values, due to the very specific growth mechanisms induced by this plasma chemistry [56], [57]. In our laboratory, such layers were developed for thin-film Si solar cells, using plasma regimes at higher pressure, 13.56 MHz excitation frequency and 200 °C (KAI-M). The layers with the highest χ_c values were obtained at a low deposition rate (<1 Å/s) [58] and were also applied in thin-film solar cells. Details are reported elsewhere [59]. These low deposition rates allow for precise deposition control of nucleation layers from SiF_4 [μc-Si:H(i_{SiF_4})] that potentially help to ensure immediate nucleation of the subsequently deposited doped μc-Si:H layers. This is of particular interest for highly sensitive interfaces as found in SHJ solar cells, however less so for applications requiring layer thicknesses typical for thin-film silicon solar cells [6].

Fluorine is a strong etching agent, used also for standard reactor cleaning. Therefore, we first assessed the impact of layers deposited by SiF_4 on τ_{eff}. For this purpose, we used textured wafers symmetrically passivated with standard a-Si:H(i) layers of various device-relevant thicknesses (10, 12.5, and 16 nm nominal, using SiH_4 as process gas). After this first step, we obtained iV_{oc} values in excess of 740 mV. This was not changed significantly by the deposition of a nominally 2-nm-thick μc-Si:H(i_{SiF_4}) nucleation overlayer (thickness estimated from the deposition rate). In fact, we saw even an increase in effective minority-carrier lifetime either related to the deposition or due to in situ reactor annealing (at 200 °C), especially in the low-to-medium excess minority-carrier density range (5×10^{14} to 1×10^{15} $1/cm^3$). The lifetime at higher minority-carrier densities ($>5 \times 10^{15}$ $1/cm^3$) remained almost unchanged, as it is already Auger-recombination limited. This result proves that our process using SiF_4 does not harm the passivation.

In a next step, we fabricated three test samples with the following stacks of layers deposited on polished (1 1 1)-oriented wafers: 1) a sandwich structure a-Si:H(i)/μc-Si:H(i_{SiF_4})/a-Si:H(i) with nominal thicknesses of 10/2/10 nm [see Fig. 1(a)] to assess the effect and thickness of the μc-Si:H(i_{SiF_4}) layer[1]; 2) a-Si:H(i)/μc-Si:H(p) (10/30 nm nominal) [see Fig. 1(b)]; and 3) a-Si:H(i_{SiF_4})/μc-Si:H(i_{SiF_4})/μc-Si:H(p) (10/2/30 nm nominal) [see Fig. 1(c)]. Using TEM on these three samples, we assess the growth mode of the μc-Si:H(i_{SiF_4}) nucleation layer and the μc-Si:H(p) (deposited from a SiH_4+H_2 plasma) with and without nucleation layer. The TEM micrograph in Fig. 1(a) shows a clear rupture between the two a-Si:H(i) layers, and it is possible to discern first nanometer-scaled crystallites forming at the interface (indicated by white arrows). This shows the potential of these highly crystalline nucleation layers. It has been argued that for SiF_4-based processes, nanocrystals may already form within the plasma leading to fast nucleation [60]. From our experiments, however, it is hard to highlight and quantify the difference between Fig. 1(b) and (c), as both samples show a clear nanocrystalline phase. Further experiments are needed to assess whether the μc-Si:H(i_{SiF_4}) layer clearly enhances the quality of the μc-Si:H(p) layers. The cell results obtained with these layers are discussed in Section III-F2.

B. Gas Variation

1) Replacing Silane by Disilane: According to literature, the silane depletion fraction is one of the fundamental factors determining the growth mode of silicon layers, *i.e.,* either μc-Si:H or a-Si:H [18], [61]. Similar conclusions were drawn for the growth of homoepitaxial silicon layers [62]. Therefore, a simple approach to facilitate the nucleation of μc-Si:H layers is the use of Si-precursor gases that are easier to dissociate compared with SiH_4 and, therefore, enable to reach high depletion regimes more easily. Disilane is known to have a lower atomic binding energy than SiH_4 and is, therefore, a good candidate [63]. Furthermore, Ar was used in the gas mixture, to facilitate the nanocrystalline growth of the layer. Excited Ar^* atoms have been proposed to transfer energy by deexcitation to the amorphous matrix, breaking weak bonds and hence enhancing nanocrystalline growth [64].

Starting with a process for a μc-SiO_x:H(p) layer at 40.68 MHz (KAI-M) [4], exhibiting $\chi_c > 40\%$ on glass with a thickness of 60 nm, the SiH_4 flow was gradually reduced while the Si_2H_6 flow was increased accordingly, keeping the total flow of atomic Si ($SiH_4 = SiH_{4\mathrm{init}} - 2 \times Si_2H_6$) and all the other deposition parameters constant.

The reactor walls were coated before each deposition with an intrinsic amorphous layer, to ensure the same starting conditions for all experiments. After this preconditioning of the reactor, the layers were deposited directly on glass substrates. We observed an increase in crystallinity of approximately 20% absolute [see Fig. 2(a)] for layer thicknesses of approximately 60 nm (measured by profilometry) deposited from a Si_2H_6 plasma. This indicates a beneficial effect of Si_2H_6 on the crystalline growth.

2) Replacing Hydrogen by Deuterium: As reported in the literature, hydrogen plays an essential role in the growth process of μc-Si:H layers. According to the surface-diffusion model [11], the adatom diffusion length of the SiH_3 radicals—that lead

[1]The sandwich structure facilitates the assessment of the layer properties with TEM.

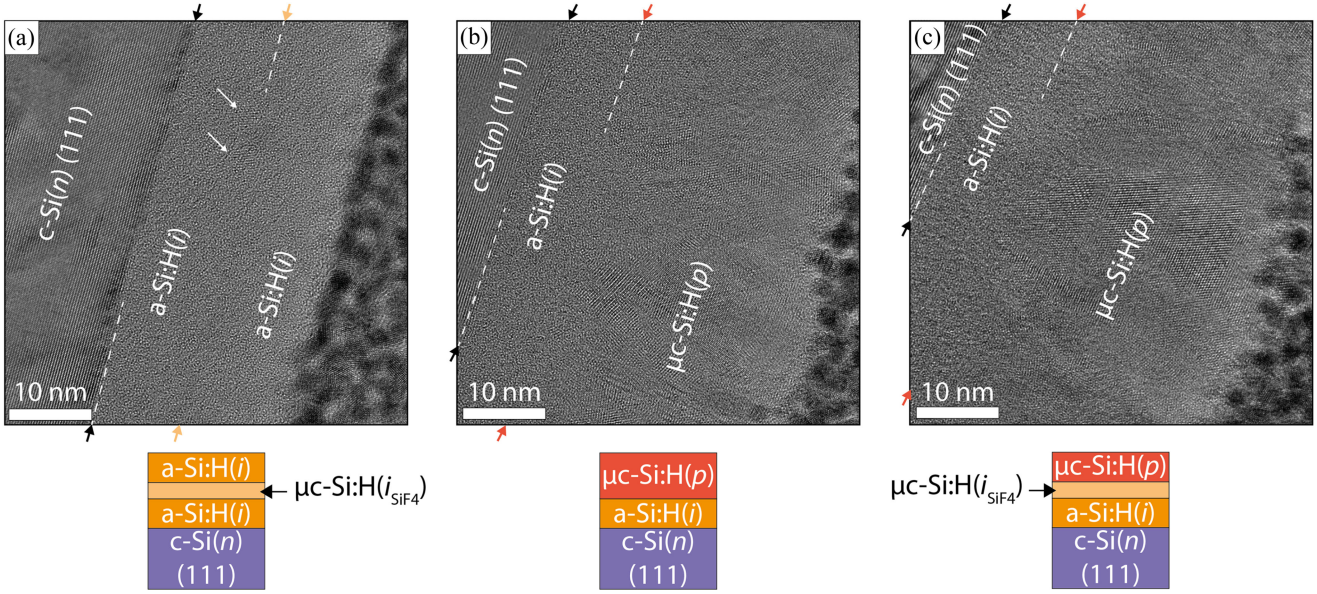

Fig. 1. Transmission electron micrographs of layers codeposited on double-side polished (1 1 1)-oriented wafers along with the textured wafers used for cell fabrication (see Section III-F2). (a) Test sample with the μc-Si:H(i) layer sandwiched between two a-Si:H(i) layers. The white arrows indicate two crystallites. Samples (b) without and (c) with the μc-Si:H(i_{SiF_4}) nucleation layer deposited from an SiF_4 plasma before the deposition of the μc-Si:H(p). The colored arrows and the dashed white lines indicate the approximate location of the interfaces.

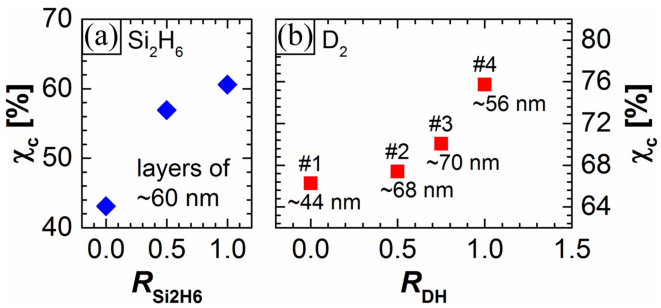

Fig. 2. Raman crystallinity (χ_c) as a function of input gas flow ratios: (a) $R_{Si2H6} = Si_2H_6/(SiH_4 + Si_2H_6)$ and (b) $R_{DH} = D_2/(D_2 + H_2)$. Thickness measured by profilometry.

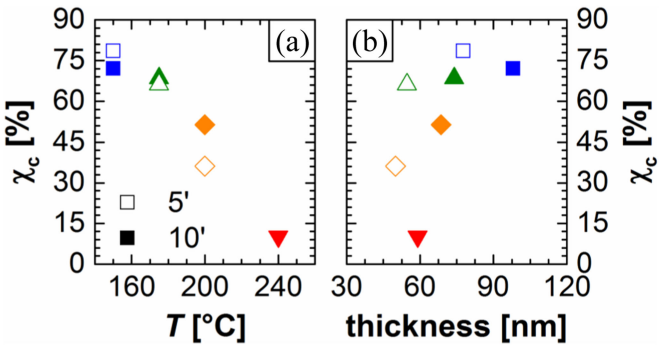

Fig. 3. Raman crystallinity (χ_c) (a) as a function of substrate temperature and the same data and (b) as a function of layer thickness. The open symbols correspond to 5-min deposition time, the solid symbols to 10 min.

to the film growth—is enhanced by the presence of hydrogen at the surface, leading to an increased probability for them to find an adequate site to attach. The selective-etching model [12], on the other hand, describes the different hydrogen etch rates for weak bonds—found at the film-growth surface and associated with the amorphous phase—and for the more stable bonds found in the crystalline phase. This will favor the growth of μc-Si:H material. Hence, replacing H_2 by D_2 may be a fruitful strategy to enhance crystalline growth, as it shows a higher etching rate due to its higher atomic mass [37].

We deposited μc-Si:H(p) layers at 40.68 MHz (Octopus I) from a $SiH_4/H_2/D_2/Ar$ plasma including TMB. These layers were deposited on glass samples coated with the a-SiO_x:H buffer layer discussed in Section III-A1. All the deposition parameters were kept constant, while the ratio between D_2 and H_2[$R_{DH} = D_2/(D_2 + H_2)$] was varied. The results are shown in Fig. 2(b). We observe a χ_c increase of more than 10% absolute comparing the layers prepared without D_2 (#1; $R_{DH} = 0$; thickness: 45 nm) and without H_2 (#4; $R_{DH} = 1$; thickness: 55 nm). For each point in Fig. 2(b), the layer thickness is indicated, to confirm that the increase in crystallinity is not merely due to an increase in film thickness.

C. Impact of Substrate Temperature on Nanocrystalline Growth

To assess the impact of the substrate temperature (T) on the nanocrystalline growth, a series of experiments were carried out in the Octopus I system. The starting point for this series was a process at 40.68 MHz yielding χ_cs of ~50% for >70-nm-thick layers, deposited at 200 °C. The gas mixture included SiH_4, H_2, TMB (0.05% in H_2), and Ar.

Keeping all the other deposition parameters constant, T was varied, while both χ_c and the layer thickness were monitored. Fig. 3(a) shows a clear trend towards lower χ_c with increasing T, which may seem counterintuitive. Fig. 3(b) shows the

TABLE I
SUMMARY OF RESULTS OBTAINED FOR P-DOPED NANOCRYSTALLINE LAYERS

substrate	frequency (MHz)	pressure (mbar)	total thickness (nm)	χ_c (%)
glass	13.56	2	∼20–30	0
glass/a-Si:H(*i*) [a]	13.56	>2	∼15	50
glass	40.68	>2	∼13	65 ± 3
glass/a-Si:H(*i*) [a]	81.36	2	∼10	55 ± 3

[a] with intrinsic μc-Si:H nucleation layer.
Layers deposited in different plasma regimes, either directly on glass or on a-Si:H(*i*) coated glass in the Octopus I (estimated error margin of ±3% absolute for χ_c).

TABLE II
SUITABILITY OF THE TESTED METHODS ON LAYER LEVEL AND FOR APPLICATION IN SHJ DEVICES

method	layer crystallinity/nucleation rate	application inSHJ devices
a-SiO_x:H(*i*) buffer	+ +	− −[a]
SiF_4 nucleation layer	+ +	+
Si_2H_6 (instead of SiH_4)	+	+
D_2 (instead of H_2)	+	+
Depo. *T* reduction	+ +	+
Depo. frequency increase	+ + +	+

[a] if applied to the hole-collecting contact.

same χ_c data as in (a) but as a function of the layer thickness. Here we see that cutting down the deposition time by half (open symbols) does not have a strong effect on the χ_c of layers deposited at lower temperatures, while at high temperatures, χ_c decreases. This indicates a reduced incubation layer thickness for the low-temperature deposition. The higher χ_c values obtained for layer deposited at lower *T* could be explained by a more efficient etching of the a-Si:H phase [65]—necessary for nucleation according to the selective etching model [12]—or by facilitated nucleation observed at lower temperatures [17]. Another explanation may be the adatom diffusivity that varies with *T* as reported in [66].

D. Influence of Plasma Excitation Frequency

Higher plasma excitation frequencies have several known beneficial effects. First, it has been shown that the nucleation of μc-Si:H material on a-Si:H is facilitated [20], and second, increasing the frequency lowers the ion energy in the plasma [67]. As reported elsewhere [37] and shown above, ion bombardment induced by a plasma can be potentially harmful to the c-Si interface and its passivation. Therefore, reducing the ion energy is especially interesting for SHJ technology, as this may reduce potential interface damage. Despite these benefits, it has been argued that increasing the excitation frequency can have a negative effect on the material quality, leading to an increase in porosity of the deposited layer [68].

We tested processes at different plasma excitation frequencies ranging from radio frequency (13.56 MHz) to very high frequency (VHF, up to 81.36 MHz), in order to identify the most suitable deposition regime for the application of μc-Si:H layers in SHJ solar cells. First, the layers were deposited either directly on glass or on a-Si:H(*i*)-coated glass and only later implemented into devices. The results that were obtained using the Octopus I are summarized in Table I. For the low-pressure (2 mbar) deposition regimes investigated at 13.56 MHz, the onset of crystalline growth was found to be strongly suppressed and the thickness of the incubation layer of material amounted to ∼20–30 nm (total layer thickness), even for intrinsic material. This onset was estimated from a series of experiments with different layer thicknesses (not shown here). This is incompatible with the application in SHJ solar cells as argued in the introduction. Typically, the layer thicknesses used in SHJ devices amounts to ∼10 nm at most. Yet, keeping the excitation frequency set to 13.56 MHz while adapting the pressure, the power, the dilution, and introducing a μc-Si:H(*i*) nucleation layer (deposited in the same deposition regime), *p*- and *n*-doped μc-Si:H layers could be obtained with device-relevant thicknesses and χ_c values on the order of 50% (obtained from SE data). The cell results obtained with these layers are reported in Section III-F3.

By increasing the frequency to 40.68 MHz, very thin yet highly crystalline doped layers were obtained on glass. However, in order to yield μc-Si:H material, the application of these layers on an a-Si:H-coated substrate necessitated surface treatments as described in Section III-A1. Hence, we increased the frequency even further to 81.36 MHz, at which μc-Si:H doped layers were obtained also on an a-Si:H-coated substrate after depositing a thin nucleation layer of μc-Si:H(*i*) under identical deposition conditions. This led to the cell results discussed in Section III-F1. The results presented here confirm earlier findings that VHF (frequencies > 40 MHz) enables the deposition of highly crystalline material [20].

E. Summary of Strategies for Nanocrystalline Layers

Table II summarizes the benefits on the nucleation rate—observed on layer level—and the applicability to SHJ solar cells of the methods discussed above.

While the deposition of an a-SiO_x:H buffer can help on layer level, this method is prone to lead to inferior cell performance, if applied to the hole-collecting side [46], which is linked to the insertion of oxide-related transport barriers into the contact stack. All the non-standard gases applied here (SiF_4, Si_2H_6, and D_2) were shown to potentially increase χ_c of the layers and are applicable to SHJ devices. Lowering the temperature does not represent a harmful measure on device level and was shown to increase χ_c. Higher deposition frequencies were shown to enable highly crystalline nanometer-scale layers, which, however, may exhibit a lower material quality [68]. Despite this latter possible drawback, as shown in the next section, devices with decent open-circuit voltage (V_{oc}) values were fabricated also at very high deposition frequencies.

All the findings presented so far are in line with previous reports [16], [18], [61], [62]. According to these results and our best knowledge, we tested the most promising and simple approaches in devices which will be presented and discussed in the following.

TABLE III
RESULTS OBTAINED FOR DIFFERENT DEPOSITION REGIMES, SYSTEMS, AND DEVICE STRUCTURES

row #	deposition regime	deposition system	contact layer front	contact layer rear	V_{oc} [mV]	J_{sc} [mA/cm^2]	*FF* [%]	*pFF*[a] [%]	η [%]
1	81.36-MHz μc-Si:H(*p*)	Octopus I	μc-Si:H(*p*)	a-Si:H(*n*)	716.7 ± 6.4	37.7 ± 0.3	72.6 ± 0.6	81.4	19.6 ± 0.3
2	reference 13.56 MHz	Octopus I	a-Si:H(*p*)	a-Si:H(*n*)	719.3 ± 0.2	36.8 ± 0.3	72.7 ± 0.5	84.1	19.2 ± 0.2
3	13.56-MHz SiF_4 μc-Si:H(*i*) 40.68-MHz μc-Si:H(*p*)	KAI-M	μc-Si:H(i_{SiF_4} *p*)	a-Si:H(*n*)	718.8 ± 1.6	35.8 ± 0.2	78.3 ± 0.1	—	20.1 ± 0.1
4	40.68-MHz μc-Si:H(*p*)	KAI-M	μc-Si:H(*p*)	a-Si:H(*n*)	719.0 ± 2.6	36.1 ± 0.3	77.2 ± 1.3	—	20.0 ± 0.3
5	reference 40.68 MHz	KAI-M	a-Si:H(*p*)	a-Si:H(*n*)	719.8 ± 2.2	36.7 ± 0.4	77.0 ± 0.6	—	20.3 ± 0.1
6	13.56 MHz	Octopus I	a-Si:H(*n*)	μc-Si:H(*ip*)	721.4 ± 0.2	37.0 ± 0.1	79.0 ± 0.3	83.9	21.1 ± 0.0
7	higher pressure & power	Octopus I	μc-Si:H(*in*)	a-Si:H(*ip*)	720.4 ± 1.0	37.1 ± 0.0	78.0 ± 0.4	82.9	20.8 ± 0.1
8	reference 13.56 MHz	Octopus I	a-Si:H(*n*)	a-Si:H(*p*)	710.3 ± 8.0	36.6 ± 0.1	76.4 ± 0.9	83.5	19.8 ± 0.4

Cell parameters given here represent the averages of three cells on the same wafer. The error margin refers to the standard deviation of the values. All devices are based on *n*-type c-Si wafers and exhibit standard a-Si:H(*i*) passivation layers on both sides. All doped μc-Si:H layers investigated here, exhibit thicknesses <30 nm on flat substrates (<17 nm on textured samples) whereas for the reference samples our standard a-Si:H(*p*) and a-Si:H(*n*) layers were used ($\sim$5–7 nm on textured samples). Note that nucleation layers are indicated by the "*i*" inside the brackets following the μc-Si:H. All the cells have an active area of approximately 23×23 mm^2, which represents the size of the TCO pad and an illuminated area of 20×20 mm^2 (masked).
[a]The *pFF* data refer to the best cells on each wafer.

F. Cell Results

Devices with an area of 2×2 cm^2 were fabricated with doped μc-Si:H layers deposited in different deposition regimes. Furthermore, we tested different structures, *i.e.,* with or without nucleation layer and hole-collecting [μc-Si:H(*p*)] layer at the front or at the rear. In the following, we first focus on the results obtained with layers deposited at high frequency. Then, we discuss the results obtained with nucleation layers deposited from a SiF_4 plasma and, finally, turn to the results obtained for the higher pressure and higher power regime at 13.56 MHz. The best cell results are summarized in Table III. Note that the error margin given in the following sections refers to the standard deviation of the measured values.

1) Cells With μc-Si:H(p) Layers Deposited at 81.36 MHz: In this regime, we deposited the μc-Si:H(*p*) layers at relatively low temperature ($\sim$180 °C) and introduced D_2 to the gas mix to obtain the highest crystallinity at a pressure of 2 mbar. The results for the best cell obtained in this regime are shown in Table III (row 1, reference row 2). The thickness of the two different *p*-type layers [reference a-Si:H(*p*) deposited at 13.56 MHz: 8.7 nm and μc-Si:H(*p*) deposited at 81.36 MHz: 9.8 nm], applied to the front of the cells, differs by only ~ 1 nm. The thickness of the a-Si:H(*p*) was measured by SE, whereas the thickness of the μc-Si:H(*p*) was estimated from the maximal deposition rate ($R_{\max}$) that was calculated using the formula given by Strahm et al. [18] (see below), assuming a hydrogen content of 10%, and represents, therefore, only an upper bound

$$R_{\max} = \frac{\Phi_{SiH_4} \cdot V \cdot m_{Si}}{A \cdot \rho}.$$

Here, Φ_{SiH_4} is the silane flow [mol/m^{3}s], V[m^3] the reactor volume, A [m^2] is the total inner surface area of the reactor, m_{Si} [kg] is the mass of a silicon atom, and ρ is the assumed density of the layer [2180 kg /m^3]. For the thickness assumed here, we obtain a reasonable deposition rate of 0.3 Å/s, which is typical for these highly nanocrystalline regimes.

Applying both of these layers to cells yielded similar V_{oc} values: (719.3 ± 0.2) mV [a-Si:H(*p*)] and (716.7 ± 6.4) mV [μc-Si:H(*p*)]. Measuring the iV_{oc} before and after the deposition of the *p*-type layers revealed a more severe drop for the device exhibiting a μc-Si:H(*p*) layer ($\sim$20 mV) while the device with an a-Si:H(*p*) layer exhibited only a small drop ($\sim$5 mV). The fact that comparable V_{oc} values have been obtained for both devices shows that the damages, induced by PECVD or sputter deposition of the TCO, can be recovered—at least partially—during the curing of the screen-printed silver paste [69]. More importantly, the μc-Si:H(*p*) layer shows a significant increase in J_{sc} of 0.9 mA/cm^2 leading to an increase of $\sim 0.4\%$ absolute in conversion efficiency. The crystallinity of the *p*-layer was confirmed by Raman spectroscopy and a χ_c of 55% was measured [see Fig. 4(a)]. Furthermore, the cell's optical performance was characterized by quantum efficiency measurements. As expected, this analysis clearly identifies the gain at short wavelengths as the reason for higher J_{sc} values [+4.8% relative in external quantum efficiency (EQE) and internal quantum efficiency (IQE) for the nanocrystalline cell [see Fig. 4(c) and (d)]. For both the a-Si:H(*p*) reference and the cell with a nanocrystalline *p*-layer, relatively high *pFF* values are obtained (see Table III). Yet, they both yield moderate *FF* values in 1-sun *J-V* measurements. Since surface passivation does not seem to be the issue here (see also the relatively high V_{oc} values), we suspect the TCO layers or the metal-paste print as possible culprits, thereby concealing the expected gain in *FF*.

2) Cells With Nucleation Layers Deposited by Silicon Tetrafluoride Plasma Chemistry: We now turn to the results obtained for cells fabricated in parallel with the layers discussed in Section III-A2, *i.e.,* with and without μc-Si:H(i_{SiF_4}) nucleation layers, deposited at 13.56 MHz (KAI-M) by SiF_4 plasma chemistry. These nucleation layers were subsequently covered by a μc-Si:H(*p*) layer, deposited in the same system at 40.68 MHz. For the devices presented here, the μc-Si:H(*p*) layer is situated at the front. From the TEM micrographs shown in Fig. 1, no apparent difference could be discerned in terms of structure and

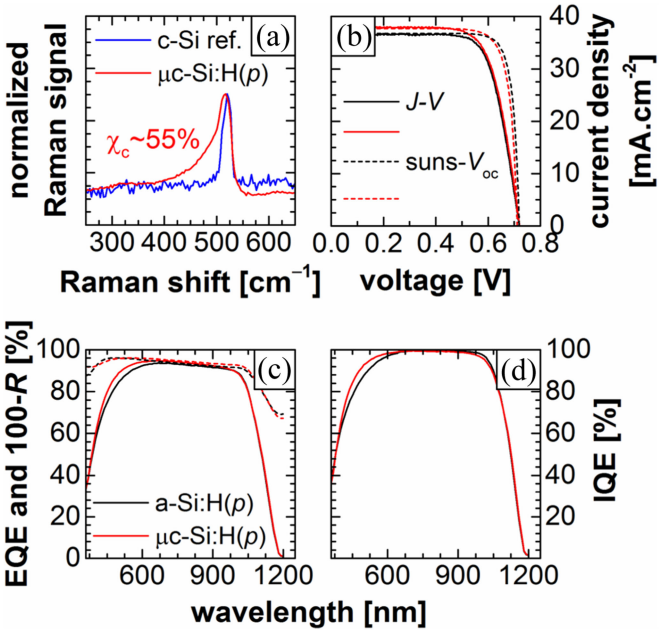

Fig. 4. (a) Raman spectra for c-Si reference and the a-Si:H(i)/μc-Si:H(p) layer stack measured directly on the c-Si wafer. The data are normalized to their peak value. (b) J-V (solid) and suns-$V_{\rm oc}$ (dashed) curves for the reference cell [standard a-Si:H(p) design] and a cell with μc-Si:H(p) hole collector. (c) EQE (solid), 100 − reflectance (dashed), and (d) IQE as a function of the wavelength.

crystallinity. The results for the two cells processed in this study are given in rows 3 and 4 of Table III (reference row 5).

In line with what was discussed earlier, the cells with μc-Si:H(p) layers do not show any significant difference to the all-a-Si:H reference in terms of $V_{\rm oc}$ and values of around 720 mV were achieved. The improvement of $J_{\rm sc}$, on the other hand, is screened by the fact that the μc-Si:H(p) layers were chosen too thick in order to ensure nanocrystalline growth. Yet, judging from the TEM micrographs [see Fig. 1(b) and (c)], there is sufficient room to thin down these layers to some extent without sacrificing their crystallinity. These results set aside—compared with the a-Si:H(p) reference—the FF values of the cells exhibiting μc-Si:H(p) layers were increased by $>1\%$ absolute. This represents a significant improvement which may be linked to the highly nanocrystalline material. Yet due to the low $J_{\rm sc}$, the conversion efficiencies of the μc-Si:H devices were all slightly lower than the reference. To which extent, the layer thickness can be optimized is subject of ongoing research. However, in order to ensure high $\chi_{\rm c}$ values at the interface to the TCO, thick μc-Si:H(p) layers may be necessary to enable high FF values which our results show. Assuming the same FF and achieving the same $J_{\rm sc}$ as obtained for the all-a-Si:H cell (lower bound) would lead to a further enhancement in conversion efficiency of up to ~0.3% absolute. We realized that avoiding the optical penalty requires hole collection at the rear. Devices of this type are presented in the following section.

3) Cells With Layers Deposited at 13.56 MHz in a Higher Power Higher Pressure Regime: Here, we present results obtained for two cells with either μc-Si:H(p) at the rear or μc-Si:H(n) at the front, both deposited at pressures of >2 mbar in the Octopus I. The doped layers on the opposite side remained amorphous. The layers were deposited from a highly diluted $SiH_4/H_2/D_2$/(TMB or PH_3) plasma at a temperature of 180 °C. For both devices, a thin μc-Si:H(i) layer was deposited as nucleation layer prior to the doped μc-Si:H layers, using identical deposition conditions, yet, without the dopant gases. It is important to note that the layers are so far not optimized in terms of thickness, doping, or crystallinity. The thickness and crystallinity of the layers were determined from ellipsometry measurements performed on codeposited a-Si:H/μc-Si:H coated flat glass samples. This yielded 9.9 nm and a crystallinity of 32.1% for the μc-Si:H(n) and 13.6 nm and 48.8% for the μc-Si:H(p) layers. These two devices are compared with an all-amorphous device with a-Si:H layer stacks exhibiting thicknesses in the range of 10 nm.

Again, both cells exhibit similar high $V_{\rm oc}$ values of around 720 mV, whereas the $J_{\rm sc}$ is slightly increased for both cells with μc-Si:H layers. However, the most impressive results obtained here are the high FF values: $(78.0 \pm 0.4)\%$ for the cell exhibiting a μc-Si:H(n) layer at the front and $(79.0 \pm 0.3)\%$ for the device with a μc-Si:H(p) layer at the rear. The detailed reasons for these high values are yet to be clarified; yet, possible explanations include high crystallinity, resulting in high doping efficiencies and hence improved contact and series resistance [52]. An additional possibility to be taken into account is the rear-side hole collection [70]. Comparing these results with the all-amorphous reference device fabricated in the same run clearly shows both the optical but also electrical benefits of μc-Si:H. However, to be fair, the reference we show here exhibits slightly lower performance (best cell: 716.7 mV, 36.7 mA/cm^2, 77.3%, and 20.4%); yet, the lower $V_{\rm oc}$ cannot account for a difference of >2% absolute in FF with respect to the best μc-Si:H device. All the results of this section are summarized in rows 6 and 7 of Table III (reference row 8).

IV. Conclusion

We have presented different strategies of how to obtain high-quality μc-Si:H material for application in SHJ solar cells. We found that the most promising process parameters to optimize are temperature and pressure. Very high frequencies can enable fast nucleation as well as, however, require especially designed reactor electrodes to avoid standing wave effects in large-scale deposition systems. Buffer or nucleation layers show the potential to help increasing the material quality; yet, they should not introduce transport-limiting factors.

With a selection of these methods and by optimizing the deposition parameters (temperature, pressure, silane dilution), we fabricated SHJ devices and obtained promising results, showing the potential of the application of μc-Si:H material in SHJ solar cells. We applied μc-Si:H(n) and μc-Si:H(p) layers without sacrificing the passivation, proven by high $V_{\rm oc}$ values in excess of 720 mV. Furthermore, compared with our standard a-Si:H layers, we observed a gain in $J_{\rm sc}$ in the order of 0.5–0.9 mA/cm^2 for layers with comparable thicknesses. Finally, using μc-Si:H(p) layers, we observed a significant increase in FF of up to 2% absolute—compared with typical values obtained for our stan-

dard devices. This may be attributed to the high crystallinity of the thick layers applied here, which advocates for hole collection at the rear in order to avoid optical losses.

Acknowledgment

The authors would like to acknowledge Meyer Burger Research and the Swiss Center for Electronics and Microtechnology for wafer preparation, S. Morel and N. Badel for screen-printing, B. Demaurex for support and fruitful discussions, and R. Tscharner, C. Bucher, J. Fonjallaz, and L. Domon for technical support.

References

[1] M. Faraji *et al.*, "High mobility hydrogenated and oxygenated microcrystalline silicon as a photosensitive material in photovoltaic applications," *Appl. Phys. Lett.*, vol. 60, p. 3289, 1992.

[2] J. Meier, R. Flückiger, H. Keppner, and A. Shah, "Complete microcrystalline p-i-n solar cell-Crystalline or amorphous cell behavior," *Appl. Phys. Lett.*, vol. 65, p. 860, 1994.

[3] T. Mueller *et al.*, "High efficiency silicon heterojunction solar cell using novel structure," in *Proc. 35th IEEE Photovoltaic Special. Conf.*, Honolulu, HI, USA, 2010, pp. 683–688.

[4] G. Bugnon *et al.*, "A new view of microcrystalline silicon: The role of plasma processing in achieving a dense and stable absorber material for photovoltaic applications," *Adv. Funct. Mater.*, vol. 22, pp. 3665–3671, 2012.

[5] K. Ding, U. Aeberhard, F. Finger, and U. Rau, "Silicon heterojunction solar cell with amorphous silicon oxide buffer and microcrystalline silicon oxide contact layers," *Phys. Status Solidi (RRL)—Rapid Res. Lett.*, vol. 6, pp. 193–195, 2012.

[6] S. Hänni *et al.*, "High-efficiency microcrystalline silicon single-junction solar cells," *Prog. Photovoltaics, Res. Appl.*, vol. 21, pp. 821–826, 2013.

[7] O. M. Ghahfarokhi, K. von Maydell, and C. Agert, "Enhanced passivation at amorphous/crystalline silicon interface and suppressed Schottky barrier by deposition of microcrystalline silicon emitter layer in silicon heterojunction solar cells," *Appl. Phys. Lett.*, vol. 104, p. 113901, 2014.

[8] T. Watahiki *et al.*, "Rear-emitter Si heterojunction solar cells with over 23% efficiency," *Appl. Phys. Express*, vol. 8, p. 021402, 2015.

[9] P. Roca i Cabarrocas *et al.*, "Stable microcrystalline silicon thin-film transistors produced by the layer-by-layer technique," *J. Appl. Phys.*, vol. 86, p. 7079, 1999.

[10] J. Mouro, A. Gualdino, V. Chu, and J. P. Conde, "Microstructure factor and mechanical and electronic properties of hydrogenated amorphous and nanocrystalline silicon thin-films for microelectromechanical systems applications," *J. Appl. Phys.*, vol. 114, p. 184905, 2013.

[11] A. Matsuda, "Formation kinetics and control of microcrystalline in μc-si:H from glow discharge plasma," *J. Non-Cryst. Solids*, vols. 59/60, pp. 767–774, 1983.

[12] C. C. Tsai, G. B. Anderson, R. Thompson, and B. Wacker, "Control of silicon network structure in plasma deposition," *J. Non-Cryst. Solids*, vol. 114, pp. 151–153, 1989.

[13] J. J. Boland and G. N. Parsons, "Bond selectivity in silicon film growth," *Science*, vol. 256, pp. 1304–1306, 1992.

[14] K. Nakamura, K. Yoshino, S. Takeoka, and I. Shimizu, "Roles of atomic hydrogen in chemical annealing," *Jpn. J. Appl. Phys.*, vol. 34, pp. 442–449, 1995.

[15] O. Vetterl *et al.*, "Intrinsic microcrystalline silicon: A new material for photovoltaics," *Sol. Energy Mater. Sol. Cells*, vol. 62, pp. 97–108, 2000.

[16] H. Fujiwara, M. Kondo, and A. Matsuda, "Stress-induced nucleation of microcrystalline silicon from amorphous phase," *Jpn. J. Appl. Phys.*, vol. 41, pp. 2821–2828, 2002.

[17] J. Robertson, "Thermodynamic model of nucleation and growth of plasma deposited microcrystalline silicon," *J. Appl. Phys.*, vol. 93, pp. 731–735, 2003.

[18] B. Strahm, A. A. Howling, L. Sansonnens, and C. Hollenstein, "Plasma silane concentration as a determining factor for the transition from amorphous to microcrystalline silicon in SiH4/H2 discharges," *Plasma Sources Sci. Technol.*, vol. 16, pp. 80–89, 2007.

[19] H. Richter and L. Ley, "Optical properties and transport in microcrystalline silicon prepared at temperatures below 400 °C," *J. Appl. Phys.*, vol. 52, p. 7281, 1981.

[20] F. Finger *et al.*, "Improvement of grain size and deposition rate of microcrystalline silicon by use of very high frequency glow discharge," *Appl. Phys. Lett.*, vol. 65, p. 2588, 1994.

[21] N. Wyrsch *et al.*, "Effect of the microstructure on the electronic transport in hydrogenated microcrystalline silicon," *J. Non-Cryst. Solids*, vols. 299–302, Part 1, pp. 390–394, 2002.

[22] M. Boccard *et al.*, "Multiscale transparent electrode architecture for efficient light management and carrier collection in solar cells," *Nano Lett.* vol. 12, pp. 1344–1348, 2012.

[23] L. Mazzarella *et al.*, "p-type microcrystalline silicon oxide emitter for silicon heterojunction solar cells allowing current densities above 40 mA/cm^2," *Appl. Phys. Lett.*, vol. 106, p. 023902, 2015.

[24] K. Ding *et al.*, "Wide gap microcrystalline silicon oxide emitter for a-SiOx:H/c-Si heterojunction solar cells," *Jpn. J. Appl. Phys.*, vol. 52, p. 122304, 2013.

[25] D. Adachi, J. L. Hernández, and K. Yamamoto, "Impact of carrier recombination on fill factor for large area heterojunction crystalline silicon solar cell with 25.1% efficiency," *Appl. Phys. Lett.*, vol. 107, p. 233506, 2015.

[26] K. Masuko *et al.*, "Achievement of more than 25% conversion efficiency with crystalline silicon heterojunction solar cell," *IEEE J. Photovoltaics*, vol. 4, no. 6, pp. 1433–1435, Nov. 2014.

[27] H. Kaya *et al.*, "Evaluation of boron and phosphorus doping microcrystalline silicon films," *Jpn. J. Appl. Phys.*, vol. 23, p. L549, 1984.

[28] S. Guha, J. Yang, P. Nath, and M. Hack, "Enhancement of open circuit voltage in high efficiency amorphous silicon alloy solar cells," *Appl. Phys. Lett.*, vol. 49, pp. 218–219, 1986.

[29] H. Stiebig, F. Siebke, W. Beyer, C. Beneking, B. Rech, and H. Wagner, "Interfaces in a-Si: H solar cell structures," *Sol. Energy Mater. Sol. Cells*, vol. 48, pp. 351–363, 1997.

[30] D. Gerlach *et al.*, "The silicon/zinc oxide interface in amorphous silicon-based thin-film solar cells: Understanding an empirically optimized contact," *Appl. Phys. Lett.*, vol. 103, p. 023903, 2013.

[31] L. Guo, M. Kondo, M. Fukawa, K. Saitoh, and A. Matsuda, "High rate deposition of microcrystalline silicon using conventional plasma-enhanced chemical vapor deposition," *Jpn. J. Appl. Phys., Part 2: Lett.*, vol. 37, pp. L1116–L1118, 1998.

[32] A. H. M. Smets, T. Matsui, and M. Kondo, "High-rate deposition of microcrystalline silicon p-i-n solar cells in the high pressure depletion regime," *J. Appl. Phys.*, vol. 104, p. 034508, 2008.

[33] Z. C. Holman *et al.*, "Current losses at the front of silicon heterojunction solar cells," *IEEE J. Photovoltaics*, vol. 2, no. 1, pp. 7–15, Jan. 2012.

[34] M. Kondo, Y. Toyoshima, A. Matsuda, and K. Ikuta, "Substrate dependence of initial growth of microcrystalline silicon in plasma-enhanced chemical vapor deposition," *J. Appl. Phys.*, vol. 80, p. 6061, 1996.

[35] E. Vallat-Sauvain *et al.*, "Influence of the substrate's surface morphology and chemical nature on the nucleation and growth of microcrystalline silicon," *Thin Solid Films*, vol. 485, pp. 77–81, 2005.

[36] S. De Wolf, A. Descoeudres, Z. C. Holman, and C. Ballif, "High-efficiency Silicon heterojunction solar cells: A Review," *Green*, vol. 2, pp. 7–24, 2012.

[37] J. Geissbühler *et al.*, "Amorphous/crystalline silicon interface defects induced by hydrogen plasma treatments," *Appl. Phys. Lett.*, vol. 102, p. 231604, 2013.

[38] S. Ghosh, A. De, S. Ray, and A. K. Barua, "Role of hydrogen dilution and diborane doping on the growth mechanism of p-type microcrystalline silicon films prepared by photochemical vapor deposition," *J. Appl. Phys.*, vol. 71, p. 5205, 1992.

[39] J.-S. Chou, W.-J. Sah, S.-C. Lee, T.-C. Chang, and J.-C. Wang, "Microcrystalline silicon deposited by glow discharge decomposition of heaviliy diluted silane," *Mater. Chem. Phys.* vol. 32, pp. 273–279, 1992.

[40] M. Tzolov, F. Finger, R. Carius, and P. Hapke, "Optical and transport studies on thin microcrystalline silicon films prepared by very high frequency glow discharge for solar cell applications," *J. Appl. Phys.*, vol. 81, pp. 7376–7385, 1997.

[41] N. Pellaton Vaucher *et al.*, "Controlled nucleation of thin microcrystalline layers for the recombination junction in a-Si stacked cells," *Sol. Energy Mater. Sol. Cells*, vol. 49, pp. 27–33, 1997.

[42] G. Bugnon *et al.*, "Silicon oxide buffer layer at the p–i interface in amorphous and microcrystalline silicon solar cells," *Sol. Energy Mater. Sol. Cells*, vol. 120, pp. 143–150, 2014.

[43] N. Layadi, P. Roca i Cabarrocas, B. Drévillon, and I. Solomon, "Real-time spectroscopic ellipsometry study of the growth of amorphous and microcrystalline silicon thin films prepared by alternating silicon deposition and hydrogen plasma treatment," *Phys. Rev. B*, vol. 52, pp. 5136–5143, 1995.

[44] S. Hamma and P. Roca i Cabarrocas, "Low temperature growth of highly crystallized silicon thin films using hydrogen and argon dilution," *J. Non-Cryst. Solids*, vols. 227–230, pp. 852–856, 1998.

[45] A. Descoeudres *et al.*, "Improved amorphous/crystalline silicon interface passivation by hydrogen plasma treatment," *Appl. Phys. Lett.*, vol. 99, p. 123506, 2011.

[46] J. P. Seif *et al.*, "Amorphous silicon oxide window layers for high-efficiency silicon heterojunction solar cells," *J. Appl. Phys.* vol. 115, pp. 0245021–0245028, 2014.

[47] A. Descoeudres *et al.*, "$>$21% Efficient silicon heterojunction solar cells on n- and p-Type wafers compared," *IEEE J. Photovoltaics*, vol. 3, no. 1, pp. 83–89, Jan. 2013.

[48] H. Wernerus, M. Bivour, L. Kroely, M. Hermle, and W. Wolke, "Characterization of ultra-thin μc-Si:H films for silicon heterojunction solar cells," *Energy Procedia*, vol. 55, pp. 310–319, 2014.

[49] C. Droz *et al.*, "Relationship between Raman crystallinity and open-circuit voltage in microcrystalline silicon solar cells," *Sol. Energy Mater. Sol. Cells*, vol. 81, pp. 61–71, 2004.

[50] R. A. Sinton and A. Cuevas, "A quasi-steady-state open-circuit voltage method for solar cell characterization," presented at the 16th Eur. Photovoltaic Sol. Energy Conf., Glasgow, U.K., 2000.

[51] P. Pernet, "Développement de cellules solaires en silicium amorphe de type "n-i-p" sur substrats souples," Ph.D. dissertation, Ecole Polytechnique Fédérale de Lausanne, Lausanne, Switzerland, 2000.

[52] L. Mazzarella *et al.*, "nanocrystalline silicon oxide emitters for silicon hetero junction solar cells," *Energy Procedia*, vol. 77, pp. 304–310, 2015.

[53] S. Kirner *et al.*, "Silicon heterojunction solar cells with nanocrystalline silicon oxide emitter: Insights into charge carrier transport," *IEEE J. Photovoltaic*, vol. 5, no. 6, pp. 1601–1605, Nov. 2015.

[54] M. Liebhaber *et al.*, "Valence band offset in heterojunctions between crystalline silicon and amorphous silicon (sub)oxides (a-SiO_x:H, $0 < x < 2$)," *Appl. Phys. Lett.*, vol. 106, p. 031601, 2015.

[55] M. Mews, M. Liebhaber, B. Rech, and L. Korte, "Valence band alignment and hole transport in amorphous/crystalline silicon heterojunction solar cells," *Appl. Phys. Lett.*, vol. 107, p. 013902, 2015.

[56] S. Kasouit, S. Kumar, R. Vanderhaghen, P. Roca i Cabarrocas, and I. French, "Fluorine and hydrogen effects on the growth and transport properties of microcrystalline silicon from SiF_4 precursor," *J. Non-Cryst. Solids*, vols. 299–302, pp. 113–117, 2002.

[57] J. C. Dornstetter, S. Kasouit, and P. Roca i Cabarrocas, "Deposition of high-efficiency microcrystalline silicon solar cells using SiF_4/H_2/Ar mixtures," *IEEE J. Photovoltaics*, vol. 3, no. 1, pp. 581–586, Jan. 2013.

[58] S. Hänni, "Microcrystalline silicon for high-efficiency thin-film photovoltaic devices," Ph.D. dissertation, Ecole Polytechnique Fédérale de Lausanne, Lausanne, Switzerland, 2014.

[59] F. Meillaud *et al.*, "Recent advances and remaining challenges in thin-film silicon photovoltaic technology," *Mater. Today*, vol. 18, pp. 378–384, 2015.

[60] S. Kasouit, J. Damon-Lacoste, R. Vanderhaghen, and P. Roca i Cabarrocas, "Contribution of plasma generated nanocrystals to the growth of microcrystalline silicon thin films," *J. Non-Cryst. Solids*, vols. 338–340, pp. 86–90, 2004.

[61] R. Bartlome *et al.*, "Practical silicon deposition rules derived from silane monitoring during plasma-enhanced chemical vapor deposition," *J. Appl. Phys.*, vol. 117, p. 203303, 2015.

[62] B. Demaurex *et al.*, "Low-temperature plasma-deposited silicon epitaxial films: Growth and properties," *J. Appl. Phys.*, vol. 116, p. 053519, 2014.

[63] B. Arkles, "Silicon compounds, silanes," in *Kirk-Othmer Encyclopedia of Chemical Technology*. Hoboken, NJ, USA: Wiley, 2000.

[64] U. K. Das, P. Chaudhuri, and S. T. Kshirsagar, "Effect of argon dilution on the structure of microcrystalline silicon deposited from silane," *J. Appl. Phys.*, vol. 80, p. 5389, 1996.

[65] F. Kaïl, A. Fontcuberta i Morral, A. Hadjadj, P. Roca i Cabarrocas, and A. Beorchia, "Hydrogen-plasma etching of hydrogenated amorphous silicon: A study by a combination of spectroscopic ellipsometry and trap-limited diffusion model," *Phil. Mag.*, vol. 84, pp. 595–609, 2004.

[66] J. E. Gerbi and J. R. Abelson, "Deposition of microcrystalline silicon: Direct evidence for hydrogen-induced surface mobility of Si adspecies," *J. Appl. Phys.*, vol. 89, p. 1463, 2001.

[67] M. Heintze and R. Zedlitz, "New diagnostic aspects of high rate a-Si:H deposition in a VHF plasma," *J. Non-Cryst. Solids*, vols. 198–200, pp. 1038–1041, 1996.

[68] G. Bugnon, "High-quality microcrystalline silicon for efficient thin-film solar cells: Insights into plasma and material properties," Ph.D. dissertation, Ecole Polytechnique Fédérale de Lausanne, Lausanne, Switzerland, 2013.

[69] B. Demaurex, S. De Wolf, A. Descoeudres, Z. C. Holman, and C. Ballif, "Damage at hydrogenated amorphous/crystalline silicon interfaces by indium tin oxide overlayer sputtering," *Appl. Phys. Lett.*, vol. 101, p. 171604, 2012.

[70] M. Bivour, H. Steinkemper, J. Jeurink, S. Schröer, and M. Hermle, "Rear emitter silicon heterojunction solar cells: Fewer restrictions on the optoelectrical properties of front side TCOs," *Energy Procedia*, vol. 55, pp. 229–234, 2014.

Authors' photographs and biographies not available at the time of publication.